Probing the Melting Transitions in Phase-Change Superlattices via Thin Film Nanocalorimetry

Jie Zhao,[∇] Asir Intisar Khan,[∇] Mikhail Y. Efremov, Zichao Ye, Xiangjin Wu, Kangsik Kim, Zonghoon Lee, H.-S. Philip Wong, Eric Pop, and Leslie H. Allen*
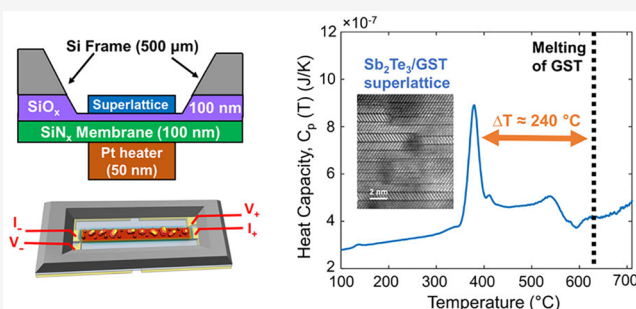
ACCESS | Metrics & More | Article Recommendations | Supporting Information

ABSTRACT: Phase-change superlattices with nanometer thin sublayers are promising for low-power phase-change memory (PCM) on rigid and flexible platforms. However, the thermodynamics of the phase transition in such nanoscale superlattices remain unexplored, especially at ultrafast scanning rates, which is crucial for our fundamental understanding of superlattice-based PCM. Here, we probe the phase transition of Sb_2Te_3 (ST)/ $Ge_2Sb_2Te_5$ (GST) superlattices using nanocalorimetry with a monolayer sensitivity (∼1 Å) and a fast scanning rate (10^5 K/s). For a 2/1.8 nm/nm Sb_2Te_3/GST superlattice, we observe an endothermic melting transition with an ∼240 °C decrease in temperature and an ∼8-fold decrease in enthalpy compared to those for the melting of GST, providing key thermodynamic insights into the low-power switching of superlattice-based PCM. Nanocalorimetry measurements for Sb_2Te_3 alone demonstrate an intrinsic premelting similar to the unique phase transition of superlattices, thus revealing a critical role of the Sb_2Te_3 sublayer within our superlattices. These results advance our understanding of superlattices for energy-efficient data storage and computing.

Nanocalorimetry of Phase-Change Superlattices

KEYWORDS: phase-change superlattice, nanocalorimetry, phase transition, melting enthalpy, superlattice interface, ultrafast scanning

Phase-change memory (PCM) stores data in two material phases, glassy and crystalline, that have different electrical conductances. PCM is a prospective memory technology given its unique characteristics of nonvolatility, a short read/write time, high endurance, and insusceptibility to ionizing radiation.[1−5] A continuous change in the conductance states of PCM resembles the behavior of synapses and may be used to realize brain-inspired computing networks.[5−8] PCM devices based on chalcogenide materials such as $Ge_2Sb_2Te_5$ (GST) undergo a reversible phase transition between crystalline (low-resistance state) and melt-quenched amorphous (high-resistance state) phases.[2] These transitions are induced by Joule heating using nanosecond electrical pulses, which, however, require a large switching current, and remain a concern for traditional PCM devices.[1,8,9]

Recently, significant progress has been reported to decrease the switching current of PCM via a superlattice (SL) platform with alternating sublayers of phase-change materials such as Sb_2Te_3/$Ge_2Sb_2Te_5$ (ST/GST),[10] $GeTe$/Sb_2Te_3,[11−13] and $TiTe_2$/Sb_2Te_3.[14] Simple epitaxial layering of these chalcogenides into a superlattice-like stack triggers a dramatic change in the transformation of the materials, i.e., switching of their phases. The reason for this effect is still not yet well-understood. One hypothesis proposed that a crystalline-to-crystalline phase transition (resistance change via subtle movement of Ge atoms), (instead of a melt−quench transition in conventional PCMs) triggers a decrease in the switching current in the $GeTe$/Sb_2Te_3 SL.[11,15] More recently, studies found that van der Waals (vdW) interfaces within SLs are responsible for the increased out-of-plane thermal resistance and the unique anisotropy of thermal and electrical conductivity, facilitating the low-power switching in PCM devices.[16−19] However, the nature of the phase transition in the SL and its corresponding thermodynamic metrics (e.g., temperature, enthalpy, and entropy) remain unexplored, especially under conditions close to those of actual PCM device operation (thin film format and fast scanning rates).

Here, we report the phase transition of phase-change ST/ GST SLs (65 nm thick) for the first time using thin film nanocalorimetry (NanoDSC).[20−25] SL samples are directly sputtered on the NanoDSC sensors without additional destructive preparations which are otherwise required for conventional calorimetry. The monolayer sensitivity (∼1 Å) of
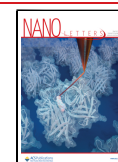
our NanoDSC enables superlattice materials probing of the same form (~60 nm thin film) as that in actual PCM devices, while its ultrafast scanning rate (10^5 K/s) captures metastable transitions in a time frame close to that of the device switching. Multiple thermodynamic fingerprints are uncovered, including a sharp endothermic transition at ~380 °C for a 2/1.8 nm/nm ST/GST SL, which provides seminal clues about the low-energy consumption and increased endurance characteristics of SL-based PCMs. This transition is ~240 °C lower than the melting (~620 °C) of bulk GST, along with an 8-fold decrease in the transition enthalpy.

Table I summarizes the names and descriptions of all of the samples in this work. They are either ST/GST SLs or

Table I. Names and Descriptions of Samples Used in This Work

sample	description of the sample
2-SL-A	2/1.8 nm/nm ST/GST superlattice (65 nm thick)
16-SL-A	(first) 16/14.4 nm/nm ST/GST superlattice (65 nm thick)
16-SL-B	(second) 16/14.4 nm/nm ST/GST superlattice (65 nm thick)
ST-A	32 nm thick ST deposited on a 4 nm ST seed layer
GST-A	28.8 nm thick GST deposited on a 4 nm ST seed layer

homogeneous ST and GST films sputtered on a SiN_x/SiO_x membrane of NanoDSC sensors (Figure 1a,b) using a self-aligned shadow mask.[27] Sensors are attached on a Si wafer using Kapton tape during the sample depositions. Samples are sputtered using the same deposition recipe as the one used to fabricate the SL-based PCM devices (described elsewhere).[10,13] Sputtering starts with a 4 nm thick seed ST layer at room temperature (RT), followed by the deposition of

subsequent GST/ST layers at 180 °C. This procedure ensures that all of the GST sublayers have a face-centered cubic (FCC) crystal structure. Similar to PCM devices, a 10 nm thick TiN capping layer is sputtered at RT to minimize oxidation and evaporation of SLs during the high-temperature NanoDSC scans.

SL stacking of the sputtered samples is verified by STEM imaging. Figure 1c reveals the atomically sharp interlayer vdW gaps inherent in the 2/1.8 nm/nm ST/GST SL deposited on a Si substrate with native SiO_x. Schematic of a 2/1.8 nm/nm ST/GST SL is also shown in Figure 1d (same as 2-SL-A on a sensor). The vdW gaps are intrinsic to the ST sublayer as they also occur in bulk ST.

Differential mode NanoDSC measurements are performed in vacuum (2×10^{-7} Torr) for a series of temperature ramping from RT to the maximum temperature (T_{max}) with a heating rate of $(1.1 \pm 0.1) \times 10^5$ K/s. A series consists of either a single scan or multiple scans with 1 s intervals, which are sufficient to passively cool samples to RT. Here, we denote each calorimetry scan as "sample ID-N_1-N_2", where N_1 is the pulse series name and N_2 is the scan number in a specific pulse series. All scans in this work are summarized in section I of the Supporting Information (SI). NanoDSC has recently revealed excellent quantitative consistency and accuracy in the measurement of the transition temperature and enthalpy for a 20 nm thick GST film upon various heating rates.[28] Operation and data analysis were further detailed in our previous works.[22,23]

Calorimetric results of all samples show complicated phase transition fingerprints that are sensitive to scanning history. Their metastability presents challenges to calorimetry measure-
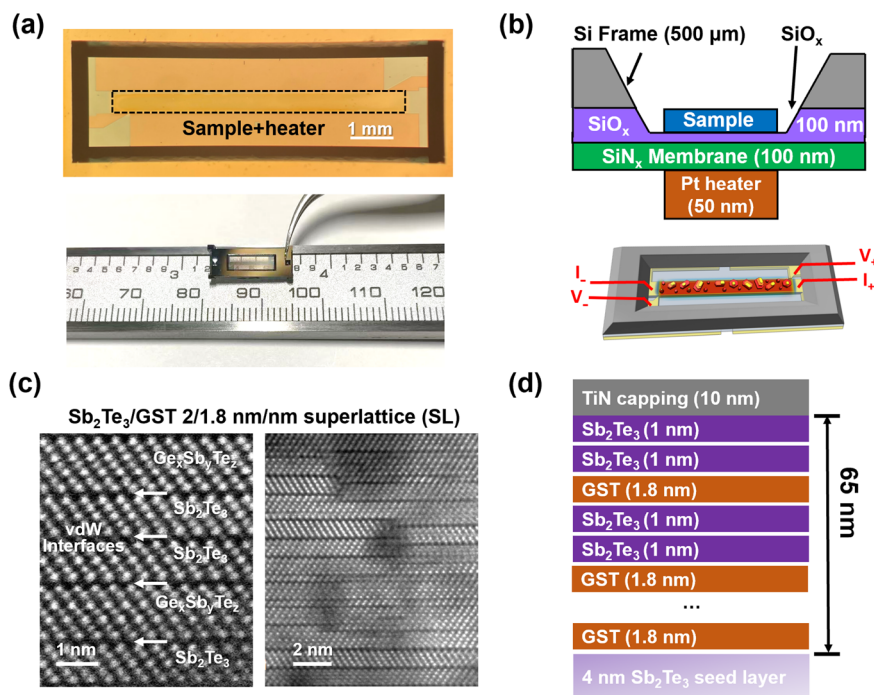

Figure 1. NanoDSC characterization of $Sb_2Te_3/Ge_2Sb_2Te_5$ (ST/GST) superlattices. (a) Optical image of a NanoDSC sensor. A caliper scale is shown for comparison. (b) Schematic of a NanoDSC sensor, including the deposited ST/GST superlattice sample (dimension not shown to scale). Reproduced with permission from ref 26. Copyright 2009 American Chemical Society. (c) High-angle annular dark-field scanning transmission electron microscopy (STEM) cross sections of the as-deposited 2/1.8 nm/nm ST/GST superlattice that shows atomically sharp vdW interfaces as well as defects such as planar grain boundaries and triple junctions, which extend across several sublayers. (d) Schematic of a 65 nm thick 2/1.8 nm/nm ST/GST superlattice stack with alternating double-layer Sb_2Te_3 and single-layer $Ge_2Sb_2Te_5$.
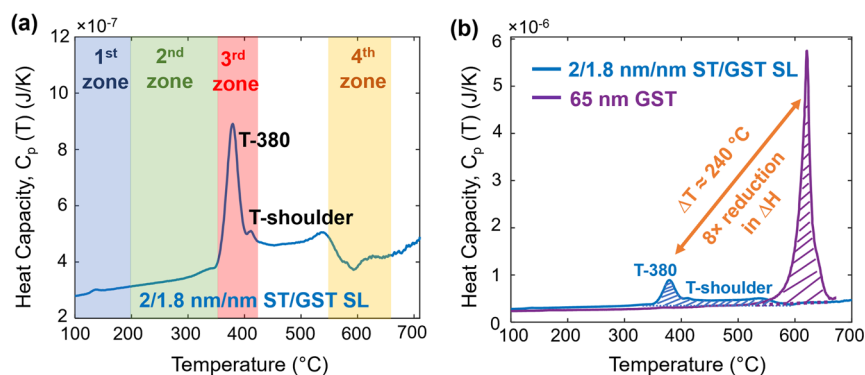
Figure 2. (a) $C_p(T)$ profile of scan 2-SL-A-6-1 (2/1.8 nm/nm ST/GST superlattice). It demonstrates a sharp endothermic transition at 380 °C (T-380) followed by a shoulder (T-shoulder) up to 560 °C, whereas minimal bulk melting signals of ST or GST are observed at ~600 °C.[28−31] Shaded regimes denote the four temperature zones discussed in this work. (b) Comparison of $C_p(T)$ profiles between the scan in panel a and that of 65 nm thick GST (equivalent to the total thickness of the SL, rescaled from 20 nm thick homogeneous GST sputtered at RT with no ST seed layer). The 65 nm GST melts at 620 °C. The T-380 peak in the superlattice (blue shaded peak) demonstrates an ~240 °C decrease in peak temperature (T_m = 380 °C) and an 8-fold decrease in the transition enthalpy (ΔH_m = 15 μJ for T-380), compared to that during the melting of GST (purple shaded peak). The overall enthalpy in SL (T-380 peak and T-shoulder; ΔH_m = 35 μJ) is also 4-fold smaller than that of GST.
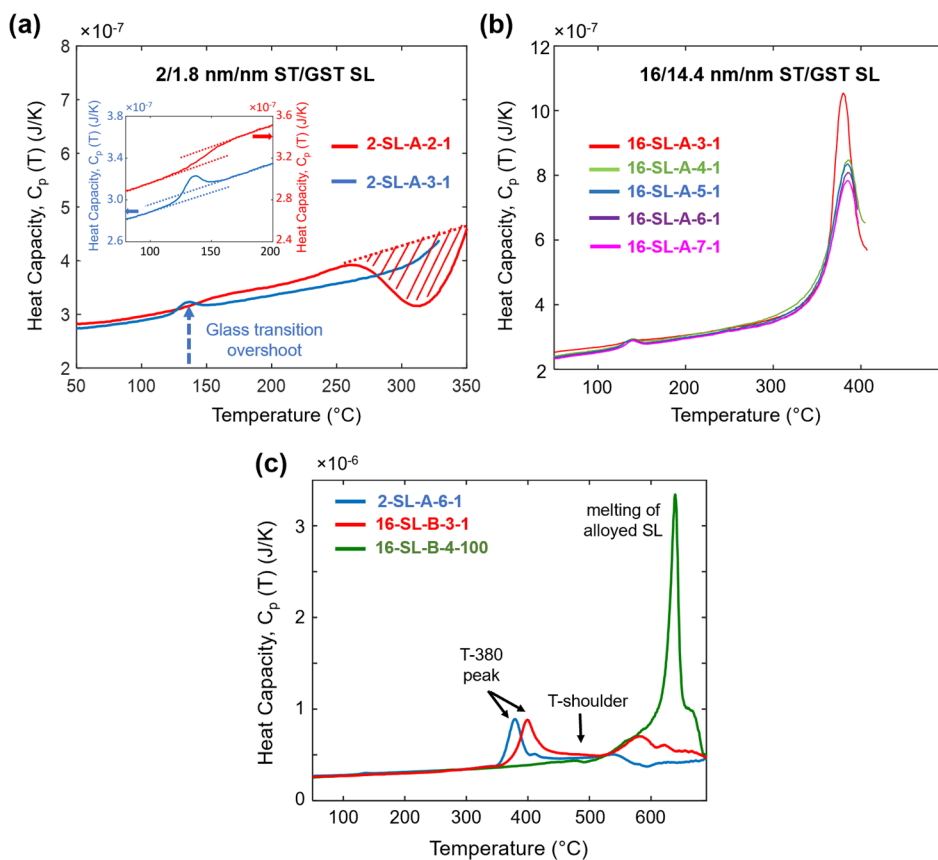

Figure 3. (a) 2-SL-A-2-1 and 2-SL-A-3-1 scans for sample 2-SL-A (2/1.8 nm/nm ST/GST superlattice) with T_{max} values of <350 °C. The inset shows the glass transition features in both curves with 80 °C < T < 200 °C. (b) $C_p(T)$ of 16-SL-A-N_1-1 (N_1 = 1−6) for a 16/14.4 nm/nm ST/GST superlattice with T_{max} values of <410 °C. (c) First $C_p(T)$ scan to 710 °C for a 16/14.4 nm/nm ST/GST superlattice (16-SL-B-3-1, red curve) and a 2/1.8 nm/nm ST/GST superlattice (2-SL-A-6-1, blue curve). After electrical annealing to 710 °C (100 pulses), a 16/14.4 nm/nm ST/GST stack (2-SL-B-4-100, green curve) shows a melting peak at 630 °C with no T-380 transition. The green curve is rescaled to compensate for the 20% decrease in heat capacity (loss of sample due to evaporation) during electrical annealing.

ments, because heating scans may simultaneously anneal and change the sample. On one hand, NanoDSC with fast scanning rate can capture the metastable transitions of SL and is key to understanding the switching of PCM devices. On the other hand, metastability introduces complexity to the scanning schedule for reliable results.

The calorimetry profile of "conditioned" 2-SL-A-6-1 (with prescans as defined below) up to 710 °C is shown in Figure 2a. A sharp endothermic melting transition at ~380 °C (T-380), followed by a shoulder pattern (T-shoulder), is observed, with minimal signs of bulk melting of the constituent ST or GST sublayers of the SL (here 2/1.8 nm/nm ST/GST). This is

unexpected because the phase diagram of bulk ST-GST predicts a melting at ~600 °C.[28−31] The T-shoulder resembles the calorimetry profile of binary systems with incongruently melting compounds.[32] The term "conditioned" here means the as-deposited SL has undergone a selected series of calorimetry scans (T_{max} = 200−350 °C) beforehand. As-deposited SL-based PCM devices also require ~1000 low-power cycles for their stable repeated switching.[10]

The T-380 transition, which we identify as mainly a crystalline-to-liquid melting transition (see section II of the Supporting Information for justifications), is the most consequential finding in this paper. It provides insight into the crystalline-to-amorphous switching transition in SL-based PCM with an 8-fold lower switching power, compared to those of conventional PCM devices.[10] Calorimetry profiles of 2-SL-A-6-1 and standard GST samples (RT sputtered) are shown in Figure 2b. An ~240 °C decrease in the melting temperature (T_m) and an 8-fold decrease in transition enthalpy (ΔH_m) are observed. The reduced enthalpy of the T-380 transition is expected from Hess' analysis[33] as a consequence of the low transition temperature (see section III of the Supporting Information). However, the reduced T_m cannot be explained by the phase diagram given the similar composition of Te (GST, 56% Te; SL, 58% Te).

Apart from T-380, a series of other transition features have been identified for a SL. They provide valuable insight into the possible presence of metastable phases (e.g., Te-rich phases) that can greatly reduce the T_m of SLs and provide further insight into the T-380 transition as we will explore below. We partition this discussion into the following four temperature zones (Figure 2a): (1) T < 200 °C, (2) 200 °C < T < 350 °C, (3) 350 °C < T < 420 °C, and (4) T > 550 °C.

The first temperature zone (T < 200 °C) demonstrates a glass transition ("T-glass") that shows negligible changes under multiple scans with T_{max} values of <180 °C. This is expected given that our SLs are deposited at 180 °C. For all 65 nm SL samples in this study, the measured heat capacity C_p(100 °C) of 279 ± 8 nJ/K agrees with the calculation (detailed in section IV of the Supporting Information).

The glass transition is observed for all SLs in this study, with a similar glass transition temperature (T_g = 140 ± 5 °C) at the first scan up to T_{max} values of <200 °C, indicating a small amount of glassy phase in the as-deposited SLs. T_g is assigned from the limiting fictive temperature analysis.[34] For example, scan 2-SL-A-2-1 (Figure 3a, red curve) demonstrates a step-like feature that resembles a "normal" glass transition with a T_g of 142 °C.

The low value of T_g deserves to be discussed further. Multiple glass phases are known for the Ge−Sb−Te system. However, a T_g of <140 °C is found only in Te-rich phases [atomic composition of Te of >85% (see section V of the Supporting Information)]. It leads to the assumption that Te-rich phases may be responsible for the observed glass transitions in the SL samples under investigation.

Because the step height of the T-glass ($\Delta C_p = C_{p\text{-liquid}} - C_{p\text{-amorphous}}$ at $T = T_g$) is proportional to the amount of the glassy phase, the quantity of the glassy Te-rich compounds can be estimated using the specific/reference ΔC_p reported for $Ge_{15}Te_{85}$ glass.[35] For instance, scan 2-SL-A-2-1 shows ΔC_p = 15 ± 1 nJ/K and thus 6 ± 0.4% of the film is glassy (detailed in section V of the Supporting Information). Such a small amount of glass agrees with the STEM observation (Figure 1c) that the as-deposited SL is mostly crystalline. It should be noted that

even with the existence of 6% Te-rich glassy phases, the overall stoichiometry for the rest of the SL remains approximately the same (Te ~ 56%) with only 2% deviations.

With regard to the second temperature zone (200 °C < T < 350 °C), a broad exothermic feature (denoted as T-exo) with a ΔH_{exo} of 5.5 μJ spanning from 250 to 350 °C is observed for 2-SL-A [scan 2-SL-A-2-1 (red curve in Figure 3a)]. This transition is irreversible because it can be observed only on the very first scan to 350 °C. From scan 2-SL-A-2-1 to the subsequent 2-SL-A-3-1 scan (red and blue curves in Figure 3a), we find the T_g of 2-SL-A shifts from 142 to 95 °C with a strong "overshoot" and the corresponding amount of glass decreases from 6% to 3% (detailed in section V of the Supporting Information).

It is reasonable to assume that the Te-rich liquid phases formed from the glass transition of the prior scan (e.g., 2-SL-A-2-1) are partially crystallized at the increased temperature, yielding the exothermic transition. This crystallization results in the smaller amount of Te-rich glass observed in the following scan (e.g., 2-SL-A-3-1). However, such a mechanism does not fully explain the strength of T-exo. ΔH_{exo} estimated solely from the reduction of Te-rich glass (3%) is only 2.0 μJ [assuming the glassy phase is $Ge_{15}Te_{85}$[35] (detailed in section V of the Supporting Information)], which is 3-fold lower than the measured ΔH_{exo}. Thus, other exothermic processes may also contribute, including the FCC to hexagonal transition, mixing, and structural relaxation.

The glass transition also developed an "overshoot" feature in scan 2-SL-A-3-1 that is demonstrated by glasses with a specific thermal history, e.g., when the cooling rate during the glass formation is lower than the heating rate of the following calorimetric scan.[36,37] This condition is typical for adiabatic NanoDSC (see section VI of the Supporting Information for a discussion of the "overshoot").

The third temperature zone (350 °C < T < 420 °C) displays the key finding of the work. The endothermic T-380 transition (as discussed above), shows up in all SL samples. With 16-SL-A as an example, its T-380 melting transition (red curve in Figure 3b) is obtained from a scan up to a T_{max} of ~410 °C after multiple low-temperature prepulses to a T_{max} of 260 °C. Subsequent scans with T_{max} values of <410 °C demonstrate excellent repeatability of the transition with a <1% loss of peak height on average. We speculate that such a reproducible transition is responsible for triggering the electrical switching in ST/GST SL-based PCM devices. From a thermal budget perspective, a single scan (30 ms heating and cooling cycle) in NanoDSC is equivalent to ~10^6 × 30 ns pulses (i.e., ~10^6 switching cycles) in PCM devices.

Te-rich compounds are the only material species that show melting at ~380 °C based on the Ge−Sb−Te phase diagram.[38] Therefore, from a calorimetry perspective, the crystalline Te-rich phases formed during the "conditioning" of SL may be a critical factor to the T-380 transition. However, they cannot be the main contributor to the T-380 transition enthalpy due to their small amount. Assuming the $Ge_{15}Te_{85}$ mentioned above as the Te-rich compound within our SL, the calculated melting enthalpy of crystalline Te-rich phases is only 2.6 μJ compared to the T-380 transition enthalpy (ΔH_m = 15−20 μJ) measured in this work (see section V of the Supporting Information). Therefore, the T-380 endothermic transition may be associated with the melting of other metastable phases not in the phase diagram. We note that both the T-380 transition and the exothermic crystallization have also been previously observed
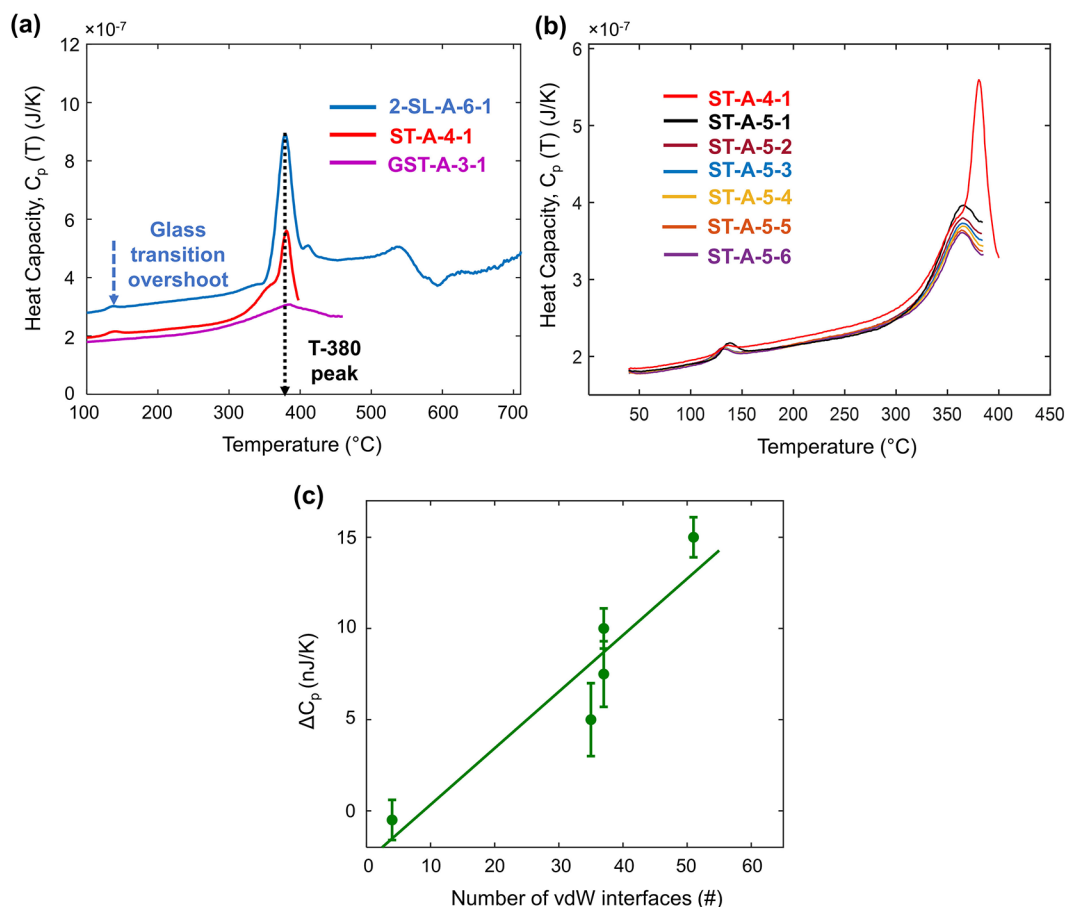
Figure 4. (a) C_p vs T scanning of 32 nm thick ST (red curve, ST-A-4-1) and 28.8 nm thick GST (purple curve, GST-A-3-1) with a 4 nm thick ST as the seed layer. Both ST and GST samples are deposited following the same deposition recipe used for the SL sublayers in this work. Scan 2-SL-A-6-1 (2/1.8 nm/nm ST/GST SL) is also included for comparison. (b) Scan ST-A-4-1 and subsequent scans ST-A-5-N_2 (N_2 = 1−6) of a 32 nm thick ST film. (c) Measured glass transition step height ΔC_p as a function of the number of vdW interfaces for five samples studied in this work. ΔC_p is measured on the first scan with a T_{max} of >200 °C for each sample, including scans 2-SL-A-2-1, 16-SL-A-2-1, 16-SL-B-2-1, ST-A-2-1, and GST-A-2-1.

for SL samples scraped from substrates using conventional calorimetry, but no quantitative enthalpy information has been reported to date.[39]

In the fourth temperature zone (T > 550 °C), we expect to observe pronounced endothermic melting transitions of ST and GST sublayers (denoted as T-bulk) at ~600 °C.[28−31] However, no such transition is detected in the conditioned SL samples during the first scan up to a T_{max} of 710 °C. As shown in Figure 3c, the 2/1.8 nm/nm ST/GST SL (2-SL-A-6-1, blue curve) shows a minimal endothermic signal in this temperature range while the 16/14.4 nm/nm ST/GST SL (16-SL-B-3-1, red curve) shows only two minor peaks. We infer that most of the SL material exists in the metastable state and melts during the T-380 and/or T-shoulder transitions, while there is a minimal amount of thermodynamically stable phases that exhibit bulk melting.

However, the ratio of the metastable and the stable phases can be reversed by applying multiple scans of SLs up to 710 °C, during which samples repeatedly melt and then recrystallize. Figure S5 illustrates such evolution of the 16-SL-B SL, where the T-380 peak progressively decreases and T-bulk gradually increases accordingly. The final scan [16-SL-B-4-100 (green curve in Figure 3c)] shows only a strong peak at 630 °C with a ΔH_m of 95 μJ, which is close to the expected ΔH_m (100 μJ) of the 65 nm SL, as detailed in section IV of the

Supporting Information. We believe that SL transforms from a metastable state to a stable bulk-like state with the material amount approximately conserved as indicated in section III of the Supporting Information. It is noted that the T-glass feature also disappears after such T_{max} = 710 °C scans. This process is further studied by TEM directly on a NanoDSC sensor[40] as detailed in section VIII of the Supporting Information.

To further understand the origin of T-380 in the SL, it is compared to its homogeneous sublayer counterparts, ST and GST. Their deposition follows the same recipe as that of the SL, including the 4 nm ST seed layer. All ST and GST samples were conditioned (prepulsed up to 250−350 °C) to start with (same as for the SLs). The follow-up scans with T_{max} values of >400 °C for ST-A (ST-A-4-1, red curve) and GST-A (GST-A-3-1, purple curve) are shown in Figure 4a.

Surprisingly, we find that ST-A (32 nm Sb_2Te_3 with a 4 nm Sb_2Te_3 seed layer) shows strong repeatable signals of both T-glass and T-380 transitions, which share temperatures similar to those of SLs (Figure 4a). Such a sharp endothermic peak at ~400 °C is also revealed by conventional calorimetry on ST nanoflakes[41−43] and bulk ST[30] (summarized in section IX of the Supporting Information), and its origin is attributed to the premelting of ST.

However, only a small T-380 transition is observed in GST-A (28.8 nm GST with a 4 nm Sb_2Te_3 seed layer) with no

measurable (~1 nJ/K sensitivity of NanoDSC[28]) T-glass transition. We attribute the presence of this small T-380 feature in GST-A to the 4 nm ST seed because GST alone does not exhibit any endothermic signal at ~400 °C as displayed in Figure 2b.

We further note that the main difference between ST-A and GST-A is that FCC GST does not have long-range vdW interfaces that are inherent in ST stacks.[44] Therefore, for all samples in this work, we correlate glass transition step height ΔC_p (measured by the first scan to $T_{max} < 200$ °C) with the number of vdW interfaces (including both homogeneous ST/ST and heterogeneous ST/GST SL types), as shown in Figure 4c. We find that the strength of the glass transition progressively increases with the number of interfaces. It suggests that vdW interfaces within the SLs could be a promoter of the Te-rich glassy structure inherent in the stacked SL layers. On the basis of the comparisons described above, we conclude that in the SLs, ST sublayers play critical roles in promoting not only the vdW interfaces but also the T-380 and glass transitions of these SLs, which could be responsible for their low-power switching operation in PCM devices.

We further discuss the mechanism of the T-380 melting transition, which is probably associated with the vdW interfaces inherent in both the ST and ST/GST SL stacks. A high density of vdW interfaces and grain boundaries may facilitate the formation of metastable phases and could be critical for the T-380 transitions. Additionally, exothermic intermixing between the ST and GST sublayers could also participate in the T-380 transition with a minor enthalpy contribution (see section X of the Supporting Information). In the end, other thin film phenomena, including size-dependent melting, may also contribute to T-380 and reduce the material melting temperature below its bulk value (see section XI of the Supporting Information). The cross-sectional TEM image of the SL on the NanoDSC sensor would provide key information to identify the metastable phase of T-380. However, because of the fragility of the 100 nm SiN$_x$ membrane, so far we have not obtained a satisfactory cross-sectional TEM sample from NanoDSC sensors, and we will keep pushing our effort in this direction.

In summary, using nanocalorimetry in Sb$_2$Te$_3$/GST superlattices, we uncovered an endothermic melting transition at ~380 °C (T-380) with an ~240 °C decrease in temperature and an ~8-fold decrease in enthalpy compared to those of the melting of GST, providing key thermodynamic insights and an original explanation of the increased endurance and low-power consumption of SL-based PCM devices. We propose that the major transition in T-380 is a crystalline-to-liquid melting transition, where other processes, including intermixing between the ST and GST sublayers could, also participate with a minor enthalpy contribution. We also uncovered a rich landscape of phase transitions, including a glass transition (T-glass), endothermic melting (T-380 and T-bulk), and exothermic effects (T-exo) in such superlattices. T-Glass suggests the presence of Te-rich glassy phases in our superlattices, which crystallized during the subsequent scans featuring an exothermic T-exo signal. As a result, the crystalline Te-rich phases could be one of the key factors for the remarkably strong and repeatable T-380 transition. High-temperature scanning of the superlattice converts its T-380 transition into T-bulk, expected from the phase diagram. These findings further show that NanoDSC is a powerful tool for

improving our understanding of superlattices for energy-efficient data storage and computing.

■ ASSOCIATED CONTENT

⊕ⓈⒾ Supporting Information

The Supporting Information is available free of charge at https://pubs.acs.org/doi/10.1021/acs.nanolett.3c01049.

Bar plots for pulsing parameters and sequences in this work (section I), justification for the crystalline-to-liquid melting transition in T-380 (section II), modeling the reduced transition enthalpy for SL based on Hess' law (section III), calculation of the expected $C_p(100$ °C$)$ for a 65 nm 2/1.8 nm/nm ST/GST SL (section IV), quantitative analysis of the glass transition and exothermic transition for scans 2-SL-A-2-1 and 2-SL-A-3-1 (section V), glass transition overshoot in a series with multiple scans (section VI), high-temperature scans for 16-SL-B (section VII), TEM results for sample 16-SL-B (section VIII), summary of previous calorimetry research ($T > 300$ °C) on Sb$_2$Te$_3$ (section IX), modeling the heat of intermixing/reaction between ST and GST sublayers in a 65 nm SL (section X), and role of Te-rich phases in T-380 (section XI) (PDF)

■ AUTHOR INFORMATION

Corresponding Author

Leslie H. Allen — *Department of Materials Science and Engineering, Coordinated Science Laboratory and Frederick-Seitz Materials Research Laboratory, University of Illinois at Urbana-Champaign, Urbana, Illinois 61801, United States;* ⓞ orcid.org/0000-0001-9323-3767; Phone: (217) 333-7918; Email: L-ALLEN9@illinois.edu

Authors

Jie Zhao — *Department of Materials Science and Engineering, Coordinated Science Laboratory and Frederick-Seitz Materials Research Laboratory, University of Illinois at Urbana-Champaign, Urbana, Illinois 61801, United States*

Asir Intisar Khan — *Department of Electrical Engineering, Stanford University, Stanford, California 94305, United States;* ⓞ orcid.org/0000-0003-4635-4667

Mikhail Y. Efremov — *College of Engineering, University of Wisconsin—Madison, Madison, Wisconsin 53706, United States;* ⓞ orcid.org/0000-0002-6379-9433

Zichao Ye — *Department of Materials Science and Engineering, Coordinated Science Laboratory and Frederick-Seitz Materials Research Laboratory, University of Illinois at Urbana-Champaign, Urbana, Illinois 61801, United States*

Xiangjin Wu — *Department of Electrical Engineering, Stanford University, Stanford, California 94305, United States*

Kangsik Kim — *Center for Multidimensional Carbon Materials, Institute for Basic Science (IBS), Ulsan 44919, Republic of Korea*

Zonghoon Lee — *Center for Multidimensional Carbon Materials, Institute for Basic Science (IBS), Ulsan 44919, Republic of Korea; Department of Materials Science and Engineering, Ulsan National Institute of Science and Technology (UNIST), Ulsan 44919, Republic of Korea;* ⓞ orcid.org/0000-0003-3246-4072

H.-S. Philip Wong — *Department of Electrical Engineering, Stanford University, Stanford, California 94305, United States*

Eric Pop − *Department of Electrical Engineering, Stanford University, Stanford, California 94305, United States; Department of Materials Science and Engineering, Stanford University, Stanford, California 94305, United States;* ⊙ orcid.org/0000-0003-0436-8534

Author Contributions

∇J.Z. and A.I.K. contributed equally to this work.

Author Contributions

A.I.K. and J.Z. conceived the idea. J.Z. and A.I.K. designed the experiments. A.I.K. performed the deposition of the samples with help from X.W. Z.Y. fabricated the sensors. M.Y.E. fabricated the NanoDSC system. J.Z. calibrated the sensors and performed the nanocalorimetry measurements (with input from Z.Y. and L.H.A.). J.Z. analyzed the data (with input from L.H.A., Z.Y., A.I.K., and M.Y.E.). K.K. and Z.L. performed high-resolution STEM. M.Y.E., J.Z., A.I.K., and L.H.A. wrote the manuscript with input from Z.Y. All authors discussed the results and edited the manuscript.

Notes

The authors declare no competing financial interest.

■ REFERENCES

(1) Wong, H.-S. P.; Raoux, S.; Kim, S.; Liang, J.; Reifenberg, J. P.; Rajendran, B.; Asheghi, M.; Goodson, K. E. Phase Change Memory. *Proceedings of the IEEE* **2010**, *98*, 2201−2227.

(2) Ovshinsky, S. R. Reversible Electrical Switching Phenomena in Disordered Structures. *Phys. Rev. Lett.* **1968**, *21*, 1450.

(3) Mittal, S.; Vetter, J. S. A Survey of Software Techniques for Using Non-Volatile Memories for Storage and Main Memory Systems. *IEEE Transactions on Parallel and Distributed Systems* **2016**, *27*, 1537−1550.

(4) Wuttig, M.; Yamada, N. Phase-Change Materials for Rewriteable Data Storage. *Nature materials* **2007**, *6*, 824−832.

(5) Raoux, S.; Xiong, F.; Wuttig, M.; Pop, E. Phase Change Materials and Phase Change Memory. *MRS Bull.* **2014**, *39*, 703−710.

(6) Sebastian, A.; Le Gallo, M.; Burr, G. W.; Kim, S.; BrightSky, M.; Eleftheriou, E. Tutorial: Brain-Inspired Computing Using Phase-Change Memory Devices. *J. Appl. Phys.* **2018**, *124*, 111101.

(7) Sebastian, A.; Le Gallo, M.; Khaddam-Aljameh, R.; Eleftheriou, E. Memory Devices and Applications for in-Memory Computing. *Nature Nanotechnol.* **2020**, *15*, 529−544.

(8) Kuzum, D.; Jeyasingh, R. G.; Lee, B.; Wong, H.-S. P. Nanoelectronic Programmable Synapses Based on Phase Change Materials for Brain-Inspired Computing. *Nano Lett.* **2012**, *12*, 2179−2186.

(9) Khan, A. I.; Kwon, H.; Islam, R.; Perez, C.; Chen, M. E.; Asheghi, M.; Goodson, K. E.; Wong, H.-S. P.; Pop, E. Two-Fold Reduction of Switching Current Density in Phase Change Memory Using Bi_2Te_3 Thermoelectric Interfacial Layer. *IEEE Electron Device Lett.* **2020**, *41*, 1657−1660.

(10) Khan, A. I.; Wu, X.; Perez, C.; Won, B.; Kim, K.; Ramesh, P.; Kwon, H.; Tung, M. C.; Lee, Z.; Oh, I.-K.; et al. Unveiling the Effect of Superlattice Interfaces and Intermixing on Phase Change Memory Performance. *Nano Lett.* **2022**, *22*, 6285−6291.

(11) Simpson, R. E.; Fons, P.; Kolobov, A. V.; Fukaya, T.; Krbal, M.; Yagi, T.; Tominaga, J. Interfacial Phase-Change Memory. *Nature Nanotechnol.* **2011**, *6*, 501−505.

(12) Khan, A. I.; Kwon, H.; Chen, M. E.; Asheghi, M.; Wong, H.-S. P.; Goodson, K. E.; Pop, E. Electro-Thermal Confinement Enables Improved Superlattice Phase Change Memory. *IEEE Electron Device Lett.* **2022**, *43*, 204−207.

(13) Khan, A. I.; Daus, A.; Islam, R.; Neilson, K. M.; Lee, H. R.; Wong, H.-S. P.; Pop, E. Ultralow−Switching Current Density Multilevel Phase-Change Memory on a Flexible Substrate. *Science* **2021**, *373*, 1243−1247.

(14) Ding, K.; Wang, J.; Zhou, Y.; Tian, H.; Lu, L.; Mazzarello, R.; Jia, C.; Zhang, W.; Rao, F.; Ma, E. Phase-Change Heterostructure Enables Ultralow Noise and Drift for Memory Operation. *Science* **2019**, *366*, 210−215.

(15) Kolobov, A. V.; Fons, P.; Saito, Y.; Tominaga, J. Atomic Reconfiguration of Van Der Waals Gaps as the Key to Switching in $GeTe/Sb_2Te_3$ Superlattices. *ACS omega* **2017**, *2*, 6223−6232.

(16) Boniardi, M.; Boschker, J. E.; Momand, J.; Kooi, B. J.; Redaelli, A.; Calarco, R. Evidence for Thermal-Based Transition in Super-Lattice Phase Change Memory. *Phys. Status Solidi RRL* **2019**, *13*, 1800634.

(17) Térébénec, D.; Castellani, N.; Bernier, N.; Sever, V.; Kowalczyk, P.; Bernard, M.; Cyrille, M.-C.; Tran, N.-P.; Hippert, F.; Noé, P. Improvement of Phase-Change Memory Performance by Means of $GeTe/Sb_2Te_3$ Superlattices. *Phys. Status Solidi RRL* **2021**, *15*, 2000538.

(18) Shen, J.; Lv, S.; Chen, X.; Li, T.; Zhang, S.; Song, Z.; Zhu, M. Thermal Barrier Phase Change Memory. *ACS Appl. Mater. Interfaces* **2019**, *11*, 5336−5343.

(19) Kwon, H.; Khan, A. I.; Perez, C.; Asheghi, M.; Pop, E.; Goodson, K. E. Uncovering Thermal and Electrical Properties of $Sb_2Te_3/GeTe$ Superlattice Films. *Nano Lett.* **2021**, *21*, 5984−5990.

(20) Lai, S.; Ramanath, G.; Allen, L.; Infante, P.; Ma, Z. High-Speed (104 C/S) Scanning Microcalorimetry with Monolayer Sensitivity (J/M2). *Applied physics letters* **1995**, *67*, 1229−1231.

(21) Olson, E. A.; Efremov, M. Y.; Zhang, M.; Zhang, Z.; Allen, L. H. The Design and Operation of a Mems Differential Scanning Nanocalorimeter for High-Speed Heat Capacity Measurements of Ultrathin Films. *J. Microelectromech. Syst.* **2003**, *12*, 355−364.

(22) Efremov, M. Y.; Olson, E. A.; Zhang, M.; Schiettekatte, F.; Zhang, Z.; Allen, L. H. Ultrasensitive, Fast, Thin-Film Differential Scanning Calorimeter. *Review of scientific instruments* **2004**, *75*, 179−191.

(23) Efremov, M. Y.; Olson, E.; Zhang, M.; Lai, S.; Schiettekatte, F.; Zhang, Z.; Allen, L. Thin-Film Differential Scanning Nanocalorimetry: Heat Capacity Analysis. *Thermochimica acta* **2004**, *412*, 13−23.

(24) Yi, F.; LaVan, D. A. Nanocalorimetry: Exploring Materials Faster and Smaller. *Applied Physics Reviews* **2019**, *6*, 031302.

(25) Nozard, H.; Schiettekatte, F. Arrhenius Behavior of Crystallization at up to 184 000 K/S in $Ge_2Sb_2Te_5$ Thin Films. *AIP Advances* **2021**, *11*, 085226.

(26) Hu, L.; Zhang, Z.; Zhang, M.; Efremov, M. Y.; Olson, E. A.; de la Rama, L. P.; Kummamuru, R. K.; Allen, L. H. Self-Assembly and Ripening of Polymeric Silver− Alkanethiolate Crystals on Inert Surfaces. *Langmuir* **2009**, *25*, 9585−9595.

(27) Kummamuru, R. K.; Hu, L.; Cook, L.; Efremov, M. Y.; Olson, E. A.; Allen, L. H. A Close Proximity Self-Aligned Shadow Mask for Sputter Deposition onto a Membrane or Cavity. *Journal of Micromechanics and Microengineering* **2008**, *18*, 095027.

(28) Zhao, J.; Hui, J.; Ye, Z.; Lai, T.; Efremov, M. Y.; Wang, H.; Allen, L. H. Exploring "No Man's Land"—Arrhenius Crystallization of Thin-Film Phase Change Material at 1 000 000 K S^{-1} Via Nanocalorimetry. *Advanced Materials Interfaces* **2022**, *9*, 2200429.

(29) Kalb, J. A. Crystallization Kinetics in Antimony and Tellurium Alloys Used for Phase Change Recording. *Aachen, Techn. Hochsch., Diss.* **2006**, *2006*, n/a.

(30) Legendre, B.; Feutelais, Y.; Didry, J. Capacite Calorifique Molaire Du Compose $Sb_{0.405}$ $Te_{0.595}$ Dans Les Etats Solides Et Liquides Entre 298 K Et 922 K. *J. Therm. Anal. Calorim.* **1988**, *34*, 345−357.

(31) Howlett, B.; Bever, M.; Misra, S. On Thermodynamic Properties of Compounds Sb_2Se_3 Sb_2Te_3+ Bi_2Te_3. *Metall. Trans.* **1964**, *230*, 1367.

(32) Rycerz, L. Practical Remarks Concerning Phase Diagrams Determination on the Basis of Differential Scanning Calorimetry Measurements. *J. Therm. Anal. Calorim.* **2013**, *113*, 231−238.

(33) Barrow, G. M. *Physical Chemistry*, 3rd ed.; McGraw-Hill: New York, 1973; pp 135−157.

(34) Seyler, R. J. *Assignment of the Glass Transition*; ASTM International, 1994; Vol. *1249*.

(35) Rocca, J.; Erazú, M.; Fontana, M.; Arcondo, B. Crystallization Process on Amorphous GeTeSb Samples near to Eutectic Point $Ge_{15}Te_{85}$. *J. Non-Cryst. Solids* **2009**, *355*, 2068−2073.

(36) Efremov, M. Y.; Olson, E. A.; Zhang, M.; Zhang, Z.; Allen, L. H. Glass Transition in Ultrathin Polymer Films: Calorimetric Study. *Phys. Rev. Lett.* **2003**, *91*, 085703.

(37) Wunderlich, B. *The Nature of the Glass Transition and Its Determination by Thermal Analysis*; ASTM Special Technical Publication; ASTM International, 1994; Vol. *1249*, p 17.

(38) Legendre, B.; Hancheng, C.; Bordas, S.; Clavaguera-Mora, M. Phase Diagram of the Ternary System Ge-Sb-Te. I. The Subternary GeTe- Sb_2Te_3-Te. *Thermochim. Acta* **1984**, *78*, 141−157.

(39) Tominaga, J.; Fons, P.; Kolobov, A.; Shima, T.; Chong, T. C.; Zhao, R.; Lee, H. K.; Shi, L. Role of Ge Switch in Phase Transition: Approach Using Atomically Controlled $GeTe/Sb_2Te_3$ Superlattice. *Japanese journal of applied physics* **2008**, *47*, 5763.

(40) Zhang, M.; Olson, E.; Twesten, R.; Wen, J.; Allen, L.; Robertson, I.; Petrov, I. In Situ Transmission Electron Microscopy Studies Enabled by Microelectromechanical System Technology. *Journal of materials research* **2005**, *20*, 1802−1807.

(41) Sun, S.; Peng, J.; Jin, R.; Song, S.; Zhu, P.; Xing, Y. Template-Free Solvothermal Synthesis and Enhanced Thermoelectric Performance of Sb_2Te_3 Nanosheets. *Journal of alloys and compounds* **2013**, *558*, 6−10.

(42) Dong, G.-H.; Zhu, Y.-J.; Cheng, G.-F.; Ruan, Y.-J. Sb_2Te_3 Nanobelts and Nanosheets: Hydrothermal Synthesis, Morphology Evolution and Thermoelectric Properties. *Journal of alloys and compounds* **2013**, *550*, 164−168.

(43) Schulz, S.; Heimann, S.; Friedrich, J.; Engenhorst, M.; Schierning, G.; Assenmacher, W. Synthesis of Hexagonal Sb_2Te_3 Nanoplates by Thermal Decomposition of the Single-Source Precursor $(Et_2Sb)_2Te$. *Chem. Mater.* **2012**, *24*, 2228−2234.

(44) Zhang, B.; Wang, X.-P.; Shen, Z.-J.; Li, X.-B.; Wang, C.-S.; Chen, Y.-J.; Li, J.-X.; Zhang, J.-X.; Zhang, Z.; Zhang, S.-B.; Han, X.-D. Vacancy Structures and Melting Behavior in Rock-Salt GeSbTe. *Sci. Rep.* **2016**, *6*, 25453.

⬚ Recommended by ACS

Supporting information

Probing the Melting Transitions in Phase-change Superlattices via Thin Film Nanocalorimetry

Jie Zhao[1,†], Asir Intisar Khan[2,†], Mikhail Y. Efremov[3], Zichao Ye[1], Xiangjin Wu[2], Kangsik Kim[4], Zonghoon Lee[4,5], H.-S. Philip Wong[2], Eric Pop[2,6], Leslie H. Allen[1,*]

[1] Department of Materials Science and Engineering, Coordinated Science Laboratory and Frederick-Seitz Materials Research Laboratory, University of Illinois at Urbana-Champaign, Urbana, Illinois, 61801, United States

[2] Department of Electrical Engineering, Stanford University, Stanford, California 94305, United States

[3] College of Engineering University of Wisconsin—Madison. Madison, Wisconsin 53706, United States

[4] Center for Multidimensional Carbon Materials, Institute for Basic Science (IBS), Ulsan 44919, Republic of Korea

[5] Department of Materials Science and Engineering, Ulsan National Institute of Science and Technology (UNIST), Ulsan 44919, Republic of Korea

[6] Department of Materials Science and Engineering, Stanford University, Stanford, California 94305, United States

[†] *These authors contributed equally to the work, Corresponding Author's Email:* L-ALLEN9@illinois.edu

I.   Bar plots for pulsing parameters/sequence in this work.

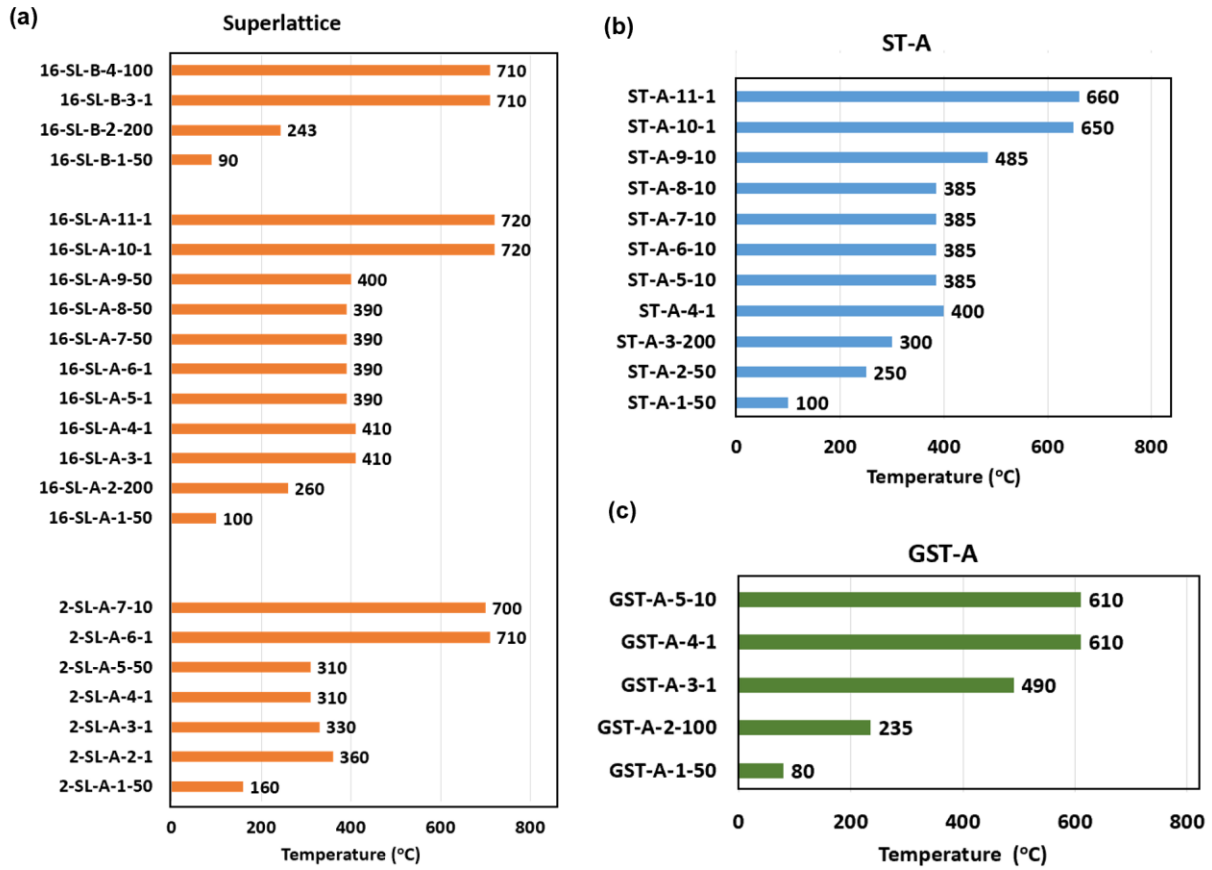
Figure S1. Bar plots for the pulsing sequence of **(a)** Superlattice, **(b)** ST-A, and **(c)** GST-A sample in this work. The y axis shows the individual pulsing series in sequence which is denoted as Sample ID-N_1-N_2, where N_1 is the pulse series ID and N_2 in this case is the maximum number of scans in each series. The x axis shows the maximum temperature in each scan series.

II.   Justification for the crystalline-to-liquid melting transition in T-380

In this work, we believe the major transition in T-380 is a crystalline-to-liquid melting transition and here are some of our justifications:

On one hand, based on TEM, the majority of the conditioned ST/GST SL in this manuscript is crystalline (**Figure S6a**). On the other hand, we expect the SL to be in the form of liquid at 710 °C based on the Ge-Sb-Te phase diagram.[1] Given "melting" is defined as the endothermic transition from crystalline to liquid phase of a material, there must be an endothermic signal in the calorimetric profile of SL assigned to "melting" in this study. Specifically, within the temperature range up to 710 °C, NanoDSC shows no other endothermic signal (**Figure 2a**) except for T-380 and the shallow T-shoulder. Therefore, we conclude that the major transition in T-380 is a crystalline-to-liquid melting transition which is further supported by its reproducibility as shown in **Figure 3b**.

In addition, the T-380 endothermic peak, which we noted here as a melting transition, is not limited to only the classic crystal-to-liquid transition of a macroscopic crystal. Broader types of transitions/interactions may contribute to the T-380 signal including eutectic melting, solid-solid transition, vacancy redistribution, strain relaxation, mixing/interdiffusion, grain-boundary melting, and size-dependent melting. However, all of these processes that participate in T-380 must be reversible/reproducible (T~400 °C) to be consistent with our measured T-380 by NanoDSC, or have a minor contribution to the enthalpy.

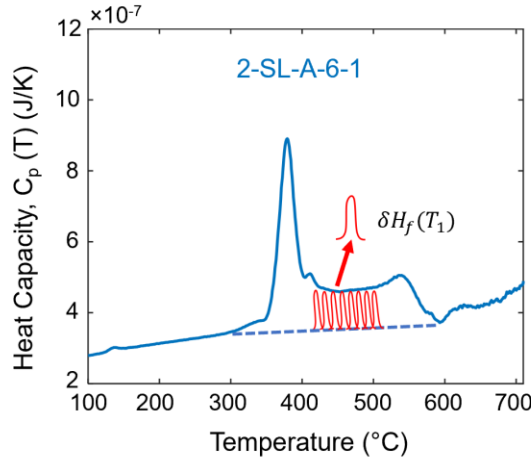III.   Modeling the reduced transition enthalpy for SL based on Hess' law.

Figure S2. Illustration of the finite element method based on Hess' law.

Here we further explore the supposition that the nature of the endothermic effect at 380 °C is melting of the ST and GST in a metastable phase and use the Hess' analysis to model the reduced enthalpy measured in this work.

As pointed out in previous calorimetry study on phase-change material $Ag_{0.055}In_{0.065}Sb_{0.59}Te_{0.29}$ (AIST)[2], crystalline-to-liquid transition exhibits reduced transition enthalpy with lower transition temperature, if the material in the undercooled liquid state (thermodynamically unstable) has higher heat capacity than the crystalline state. Therefore, the reduced melting enthalpy measured in this work for superlattice could be related with its ~240 °C decrease in melting temperature.

We further investigate this supposition quantitatively. According to Hess' law[3], for melting transition at T_1 (in this study, variable T_1 is in the range of 300 °C -600 °C), the molar melting enthalpy $\Delta h_f(T_1)$ can be expressed as:

$$\Delta h_f(T_1) = \Delta h_f(T_{bulk}) - \int_{T_1}^{T_{bulk}} (cp_{liquid}(T) - cp_{soild}(T))dT \tag{1}$$

where $cp_{liquid}(T)$ and $cp_{soild}(T)$ are the molar heat capacity for undercooled liquid and solid phases. If we assume the molar heat capacity difference ($d_{cp} = cp_{liquid}(T) - cp_{soild}(T)$) is a constant against temperature, based on equation (1):

$$\Delta h_f(d_{cp}, T_1) = \Delta h_f(T_{bulk}) - d_{cp} \times (T_{bulk} - T_1) \tag{2}$$

Our purpose is to numerically calculate the average d_{cp} for SL in the 300 °C-600 °C temperature interval. Since the SL in this study exhibits continuous endothermic signal, we use finite-element method assuming that the continuous signal is the convolution of many small

endothermic peaks with enthalpies of $\delta H_f(T_1)$ as shown in **Figure S2**. $\delta H_f(T_1)$ can be calculated directly from the calorimetric signal:

$$\delta H_f(T_1) = C_p(T_1)\delta T_1 \tag{3}$$

The corresponding amount of material transformed, $\delta n(T_1)$, can be obtained using equation (2):

$$\delta n(T_1) = \frac{\delta H_f(T_1)}{\Delta h_f(T_{bulk}) - d_{cp} \times (T_{bulk} - T_1)} = \frac{C_p(T_1)\delta T_1}{\Delta h_f(T_{bulk}) - d_{cp} \times (T_{bulk} - T_1)} \tag{4}$$

Therefore, by integrating both side of equation (4), we have:

$$\int_{T_{onset}=300^oC}^{T_{endset}=600^oC} \frac{C_p(T_1)}{(\Delta h_f(T_{bulk}) - d_{cp} \times (T_{bulk} - T_1))} dT_1 = n_0 \tag{5}$$

where n_0 is the total amount of material in the sample. Therefore, d_{cp} can be calculated by integrating the $C_p(T)$ measured experimentally. Since GST and ST have similar melting transition characteristic, the ST/GST superlattice can be considered as a uniform compound for the calculation.

For scan 2-SL-A-6-1, if we use the value of bulk GST (T_m = 620 °C and Δh_f = 14.7 kJ/mol-atom)[2] for equation (5), the method reveals d_{cp}=44.3 J/K/mol (cp_{soild} =27.2 J/(K·mol-atom), cp_{liquid} =71.5 J/(K·mol-atom)). In other words, the reduced molar enthalpy revealed in this work can be explained by assuming liquid state SL has a 2.6× higher heat capacity compared to solid state (cp_{liquid}=A× cp_{soild}, A=2.6). In this work, A=2.6 obtained based on finite-element method is reasonable compared to A=2.0-2.8 measured in liquid telluride such as AIST and Ge$_{15}$Te$_{85}$.[2, 4-5] It needs to be pointed out that the d_{cp} calculated in this method is the average excess specific heat capacity between undercooled liquid and crystalline state (300 °C-600 °C) and cannot fully represent the non-constant d_{cp} as shown in previous study.[2, 4-5]

IV.   Calculation of expected C_p (100 ℃) for 65 nm 2/1.8 nm/nm ST/GST SL

For the 65 nm 2/1.8 nm/nm ST/GST SL deposited on the NanoDSC sensor (sensing regime 2.25×10^{-6} m^2), based on a lattice constant[6] of $\boldsymbol{a}$=4.22 Å as well as the superlattice configuration shown in **Figure 1d**, the total amount of ST and GST can be calculated as 3.78 nmol and 3.02 nmol. Reported specific heat for ST and GST at 100 ℃ are 26.2 J/(K·mol-atom) and 27.2 J/(K·mol-atom) respectively, which gives a total heat capacity of 181 nJ/K.[7-8] For the 10 nm TiN capping layer, based on a density of 5.4×10^3 kg/m^3 and a specific heat capacity of 43 J/K/mol-atom, it gives a total heat capacity of 84 nJ/K.[9] Therefore, the overall heat capacity expected for the 65 nm 2/1.8 nm/nm ST/GST SL is 265 nJ/K, which is within 6% compared with the value (C_p (100 ℃) = 279 ± 8 nJ/K) measured for 65 nm superlattices in this work. Therefore, the value of C_p (100 ℃) measured by NanoDSC confirms the amount of material deposited on the sensor. Based on an molar melting enthalpy of 14.7 kJ/mol-atom for GST[2], the expected melting enthalpy of SL after high-temperature cycling/alloying is 100 μJ.

V. Quantitative analysis on the glass transition and exothermic transition for scan 2-SL-A-2-1 and 2-SL-A-3-1

Table S1. Glass transition characteristics by NanoDSC

Glass transition temperature for scan 2-SL-A-2-1, $T_{g\text{-as}}$	142± 2	ºC
Glass transition temperature for scan 2-SL-A-3-1, $T_{g\text{-relaxed}}$	95±2	ºC
Heat capacity step height for scan 2-SL-A-2-1, $\Delta C_{p\text{-as}}$	15±1.1	nJ/ K
Heat capacity step height for scan 2-SL-A-3-1, $\Delta C_{p\text{-relax}}$	7±0.5	nJ/ K

Table S2. Bulk properties of glassy $Ge_{15}Te_{85}$

[10]Specific glass transition step height, Δc_p,	0.31	J/(g·K)
[10]Crystallization enthalpy, $\Delta h_c(T = 200\ ^oC)$	43	J/g
[11]Glass transition temperature for as-deposited glass, $T_{g\text{-as}}$	135	ºC
[11]Glass transition temperature for fully relaxed glass, $T_{g\text{-relaxed}}$	105	ºC

Table S3. Bulk properties of crystalline $Ge_{15}Te_{85}$

[12]Melting point, T_m	377	ºC
[12]Melting enthalpy, $\Delta h_m(T = 377\ ^oC)$	91.22	J/g
[13]Molar volume, v_m	21×10^{-6}	m^3/mol
Molar mass, M	119.3	g/mol

Table S4. Calculated results

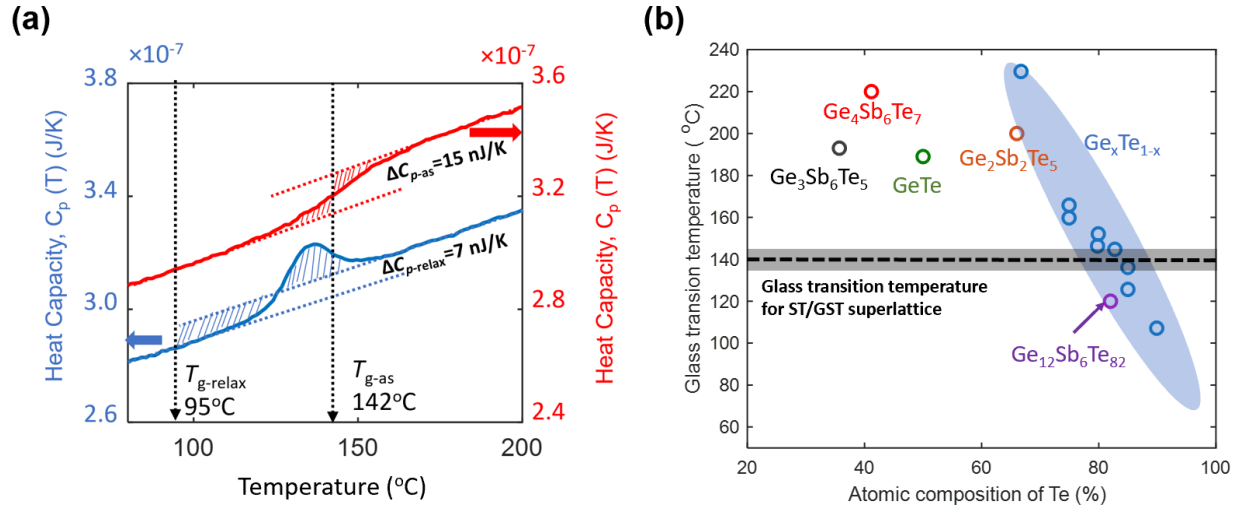|		
Equivalent thickness of glassy $Ge_{15}Te_{85}$ before the scan 2-SL-A-2-1 based on ΔC_p	4.1	nm
Equivalent thickness of glassy $Ge_{15}Te_{85}$ after the scan 2-SL-A-2-1 based on ΔC_p	1.9	nm
Estimated crystallization enthalpy of $Ge_{15}Te_{85}$	2.0	μJ
Estimated melting enthalpy of $Ge_{15}Te_{85}$	2.6	μJ

Figure S3 (a) Illustration of data analysis method to obtain glass transition temperature (T_g, based on limiting fictive temperature) and step height (ΔC_p) for scan 2-SL-A-2-1 and the subsequent 2-SL-A-3-1. **(b)** Glass transition temperature of as-deposited telluride glass in Ge-Sb-Te system. Including $Ge_3Sb_6Te_5$[14], $Ge_4Sb_6Te_7$[15], $GeTe$[16], $Ge_2Sb_2Te_5$[17], $Ge_{12}Sb_6Te_{82}$[18] and Ge_xTe_{1-x}[5]. The range of glass transition temperature for ST/GST superlattice measured in this study is also given as indicated by the black dashed regime.

In **Figure 3a**, the $C_p(T)$ of SL demonstrates characteristic glass transition for glassy material. The glass transition temperature (T_g) is assigned with the limiting fictive temperature. Glass transition step height ($\Delta C_p = C_{p\text{-liquid}} - C_{p\text{-amorphous}}$ at $T = T_g$) is defined as heat capacity difference before and after glass transition. The glass transition attributes measured by NanoDSC for 2-SL-A are summarized in **Table S1**. By comparing 2-SL-A-2-1 and the subsequent 2-SL-A-3-1 scan (red and blue curves in **Figure S3a**), we find that T_g of 2-SL-A shifts from 142 °C to 95 °C with a strong "overshoot" and the corresponding amount of glass reduces by ~50 % based on ΔC_p. The reduced T_g is expected as the glass obtained from a supercooled liquid is supposedly more relaxed than its gas-phase deposited amorphous counterpart.

We notice that the glass transition characteristics in SL are similar to that of Te-rich phase in Ge-Sb-Te system. For example, as-deposited $Ge_{15}Te_{85}$ exhibits step-like glass transition with T_g~135 °C and the value is reduced to 105 °C with dramatic overshoot after proper annealing.[11] In surveying a wide range of available values of T_g in the Ge-Sb-Te ternary system (See **Figure S3b**) the only compounds that shows T_g values below <140 °C are Te-rich phases (atomic composition of Te > 85%). Therefore, we proposed that there could be Te-rich glass in the as-deposited SLs.

Before we conduct quantitative analysis, we first calculate the equivalent thickness of one-gram $Ge_{15}Te_{85}$ based on a sensing regime area of 2.25×10^{-6} m^2 for NanoDSC sensor:

$$d_m = \frac{m}{M} \times \frac{v_m}{S} = \frac{1\,\text{g}}{119.3\,\text{g/mol}} \frac{21 \times 10^{-6}\,\text{m}^3/\text{mol}}{2.25 \times 10^{-6}\,\text{m}^2} = 0.078\,m \tag{6}$$

Therefore, one gram of $Ge_{15}Te_{85}$ corresponds to 0.078 m thick $Ge_{15}Te_{85}$ film on NanoDSC sensor.

Assuming the glassy phase in the SL is $Ge_{15}Te_{85}$, we can calculate the amount of Te-rich glass before and after the scan 2-SL-A-2-1 to 350 °C, based on the specific glass transition step height Δc_p measured in bulk $Ge_{15}Te_{85}$ as well as other data shown in **Table S2, S3**.

The mass of glassy $Ge_{15}Te_{85}$ in SL before the scan 2-SL-A-2-1 is:

$$m = \frac{\Delta C_{p-as}}{\Delta c_p} = \frac{15 \times 10^{-9} \text{ J/°C}}{0.29 \text{ J/(g} \cdot^o \text{ C)}} = 5.2 \times 10^{-8} \text{g} \tag{7}$$

which equals to a thickness of:

$$d = m \times d_m = 5.2 \times 10^{-8} g \times 0.078 \text{ m/g} = 4.1 \text{ nm} \tag{8}$$

This value is ~ 6% of the 65 nm SL. The mass of glassy $Ge_{15}Te_{85}$ after the scan 2-SL-A-2-1 is:

$$m = \frac{\Delta C_{p-relax}}{\Delta c_p} = \frac{7 \times 10^{-9} \text{ J/°C}}{0.29 \text{ J/(g} \cdot^o \text{ C)}} = 2.4 \times 10^{-8} \text{ g} \tag{9}$$

which equals to a thickness of:

$$d = m \times d_m = 2.4 \times 10^{-8} \text{ g} \times 0.078 \text{ m/g} = 1.9 \text{ nm} \tag{10}$$

This value is ~ 3% of the 65 nm SL. The reduction of glassy material implies that part of the glassy phase is crystallized during the scan 2-SL-A-2-1 to 350 °C, which could contribute to the exothermic peak at 300 °C as shown in **Figure 3a**. Based on this assumption, we can calculate the crystallization enthalpy based on the amount of Te-rich phases($Ge_{15}Te_{85}$) reduced during the first scan (2-SL-A-2-1).

First, we calculate the specific crystallization heat of $Ge_{15}Te_{85}$ at 300 °C. According to previous research[10,12], $\Delta h_c(200\,^o\text{C}) = 43 \text{ J/g}$ and $\Delta h_m(377\,^o\text{C}) = 91.22 \text{ J/g}$, Therefore, according to Hess' law in equation (2):

$$\Delta h_c(300^o\text{C}) = \Delta h_m(377\,^o\text{C}) - \frac{\Delta h_m(377\,^o\text{C}) - \Delta h_c(200^o\text{C})}{(377\,^o\text{C} - 300^o\text{C})/(377\,^o\text{C} - 200^o\text{C})} = 70 \text{ J/g} \tag{11}$$

The crystallization enthalpy of $Ge_{15}Te_{85}$ is:

$$m = 2.8 \times 10^{-8} g \times 70 \text{ J/g} = 2.0 \text{ }\mu J \tag{12}$$

In other words, the crystallization of Te-rich phases during the first scan to 350 °C (2.1 nm, 2-SL-A-2-1) contributes only 36% of the exothermic peak (5.5 μJ) measured as shown in **Figure 3a**. Therefore, the nature of the T-exo transition in scan 2-SL-A-2-1 could be more complicated. This is further supported by the peak width (50 K) which is too broad to be considered as a

single-step crystallization transition compared with the sharp (peak width 22 K) crystallization peak in our previous research on GST.[7]

The Te-rich phase could also be related with the T-380 transition revealed in this work since it is the only material species that shows low melting points at ~380 °C according to the Ge-Sb-Te phase diagram.[19] Based on a $\Delta h_m = 91.22$ J/g reported for $Ge_{15}Te_{85},$[12] the Te-rich phase crystallized during the first scan to 350 °C may contribute to the melting enthalpy of T-380 peak with a value:

$$\Delta H_m = 2.8 \times 10^{-8} g \times 91.22\ J/g = 2.6\ \mu J \tag{13}$$

The calculated results in this section are summarized in **Table S4**.

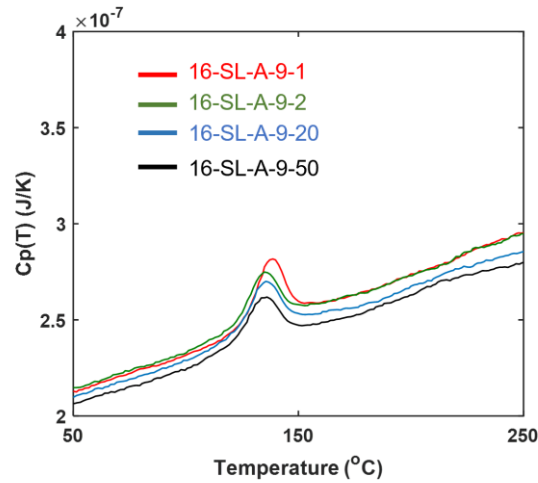VI.   Glass transition overshoot in a series with multiple scans

Figure S4. Scan 16-SL-A-9-N_1, N_1=1, 2, 20, and 50. The first scan in this series has a more pronounced overshoot

The glass transition overshoot is observed for various superlattice samples (sample 2-SL-A in **Figure 2a**, 16-SL-A in **Figure 3b**) as well as the ST sample (sample ST-A in **Figure 4a**) in this study. We also find that, for a certain multiple-scan series, the first scan in the series has more pronounced overshoot than all subsequent scans (See **Figure S4**). It is also typical for glass transitions because the period of time between series is much more than the 1 s interval between scans in the same series. Deeper glass relaxation between series causes increased overshoot.

VII.   High-temperature scans for 16-SL-B

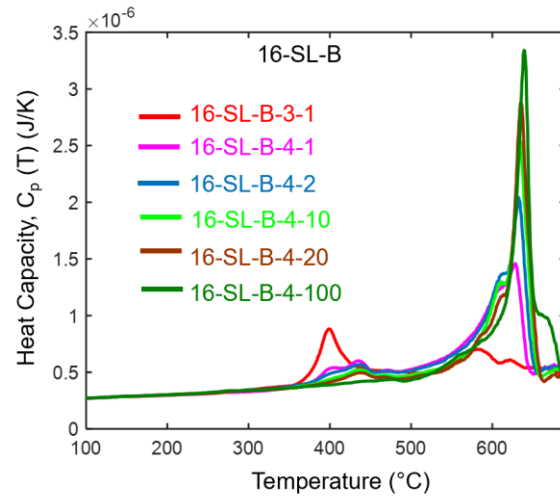**Figure S5**. The progressive evolution of the $C_p(T)$ during high-temperature scans to 710 °C for 16/14.4 nm/nm ST/GST superlattice (sample 16-SL-B). The intensity is rescaled to compensate for the decrease in heat capacity (maximum 20 %, sample amount loss due to evaporation) during the electrical cycling.

'

VIII.   TEM results for sample 16-SL-B

(a)

(b)

**16-SL-B sample
before the scan
16-SL-B-3-1**

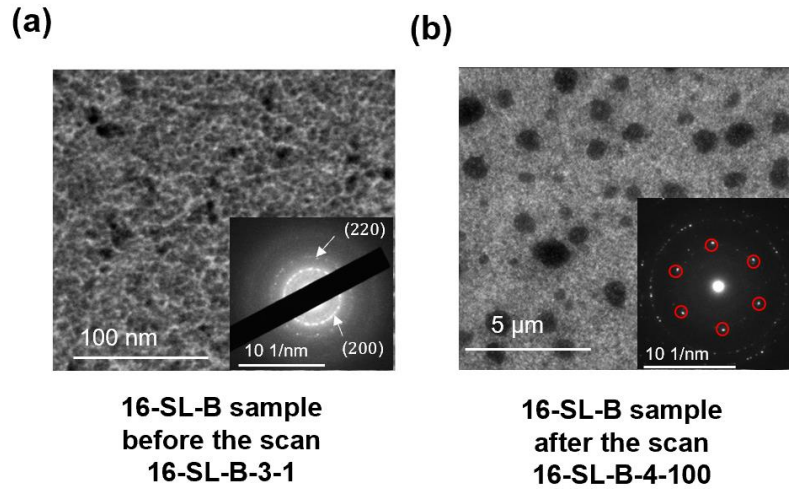**16-SL-B sample
after the scan
16-SL-B-4-100**

Figure S6. Bright field TEM images of 16-SL-B sample on NanoDSC sensor (a) before the scan 16-SL-B-3-1 and (b) after the scan 16-SL-B-4-100 respectively. The relatively large background noise comes from the scattering of the relatively thick 100 nm SiN$_x$ membrane. The inset shows the corresponding electron diffraction patterns.

The progressive evolution of SLs during high-temperature scans is also studied by planar TEM directly on the NanoDSC senosr[20] as shown in **Figure S6.** Before the scan 16-SL-B-3-1 (which is the first scan to show the T-380 peak in this sample), the conditioned SLs demonstrate uniform and continuous in-plane polycrystalline morphology (grain size ~10 nm, consistent with the density of planer grain boundary and triple junction in **Figure 1c**). The corresponding selected area diffraction (SAD) pattern reveals expected (200) and (220) diffraction peaks of GST/ST as shown in **Figure S6a**. After the high-temperature scan 16-SL-B-4-100, the continuous film forms individual ~500 nm nanoparticles (due to the dewetting between SiO$_x$ and Ge$_x$Sb$_y$Te$_z$), which exhibit a single crystalline nature (SAD pattern in **Figure S6b**).

IX.　　Summary of previous calorimetry research ($T>300\,^{\circ}\mathrm{C}$) on Sb_2Te_3.

Sample	Method	Premelting peak	Premelting shoulder	Tm	Hm
Sb_2Te_3 nanosheets[21]	DSC	Sharp peak at 418.3 $^{\circ}\mathrm{C}$ with peak intensity 10% of bulk melting.	N.A	613.3 $^{\circ}\mathrm{C}$	N.A
Sb_2Te_3 Nanoplates[22]	DSC	Sharp peak at 407 $^{\circ}\mathrm{C}$ with peak intensity 12% of bulk melting.	N.A	609 $^{\circ}\mathrm{C}$	N.A
Sb_2Te_3 nanobelts and nanosheets[23]	DSC	Sharp peak at 417 $^{\circ}\mathrm{C}$.	N.A	N.A	N.A
Zone refined Sb_2Te_3 single crystals[24]	DSC	No sharp peak	C_p for shoulder is 10 % higher than C_p at RT	618.5 $^{\circ}\mathrm{C}$	19.8 kJ/mol
Bulk $Sb_{0.405}Te_{0.595}$ single crystals[25]	Drop calorimetry	Sharp peak at 380 $^{\circ}\mathrm{C}$ with peak intensity 1.5 % of bulk melting.	C_p for shoulder is 17 % higher than C_p at RT	616.5 $^{\circ}\mathrm{C}$	20.4 kJ/mol
ST-A, this work	NanoDSC	Sharp peak at 380 $^{\circ}\mathrm{C}$ with peak intensity 13 % of expected bulk melting.	C_p for shoulder is 70 % higher than C_p at RT	N.A	N.A

X. Modeling the heat of intermixing/reaction between ST and GST sublayers in 65 nm SL

Based on the GeTe-Sb$_2$Te$_3$ phase diagram, several line compounds exist between Ge$_2$Sb$_2$Te$_5$ and Sb$_2$Te$_3$, including Ge$_1$Sb$_2$Te$_4$ and Ge$_1$Sb$_4$Te$_7$. Therefore, Ge$_2$Sb$_2$Te$_5$ and Sb$_2$Te$_3$ sublayers in SL have thermodynamic tendency to react/intermix with each other and could happen in SL sample in this study.

However, we deduce that intermixing/reaction alone cannot be the origin of T-380 peak because such transition is exothermic and irreversible with minor transition enthalpy. The following reaction between Sb$_2$Te$_3$ and Ge$_2$Sb$_2$Te$_5$ is suggested based on the phase diagram[1] of GeTe-Sb$_2$Te$_3$:

$$2Sb_2Te_3+Ge_2Sb_2Te_5=Ge_1Sb_2Te_4+Ge_1Sb_4Te_7$$
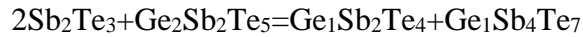
Based on previous DFT[26] calculation, such reaction is exothermic, and the heat of mixing is only ~ 0.6 μJ for 65 nm SL. In contrast, the transition enthalpy of T-380 measured in this work is 15 μJ (20 μJ for T-shoulder and 5.5 μJ for exothermic transition in **Figure 3a**).

On the other hand, the intermixing could happen during the conditioning of SL. The associated exothermic DSC signal (**Figure 3a**) may be critical in forming the metastable material infrastructure which is responsible for the T-380 transition.

XI.   The role of Te-rich phases in T-380

In the main manuscript, we conclude that Te-rich phases are critical factors for the T-380 transition but cannot be solely accounted for the T-380 transition enthalpy. The role of crystalline Te-rich phases could be related with the size-dependent melting. Since there are high density of vdW interfaces/grain boundaries in the SL, molten Te-rich phases (liquid) may change the interface energy for grains/sublayers in the SL with a value different from that of the solid phase. Therefore, the Te-rich phases with low melting points may facilitate the size-dependent melting which also depends on interface energy.[27]

Reference

1.   Bordas, S.; Clavaguer-Mora, M.; Legendre, B.; Hancheng, C., Phase Diagram of the Ternary System Ge-Sb-Te: Ii. The Subternary Ge-GeTe-Sb$_2$Te$_3$-Sb. *Thermochimica acta* **1986**, *107*, 239-265.

2.   Kalb, J.; Spaepen, F.; Wuttig, M., Calorimetric Measurements of Phase Transformations in Thin Films of Amorphous Te Alloys Used for Optical Data Storage. *Journal of applied physics* **2003**, *93*, 2389-2393.

3.   Barrow, G. M., Physical Chemistry' 3rd Edn. **1973**, 135-157.

4.   Schmid, J.; Sommer, F., Heat Capacity of Liquid Eutectic Tellurium Alloys. *Berichte der Bunsengesellschaft für physikalische Chemie* **1998**, *102*, 1279-1283.

5.   deNeufville, J. P., Chemical Aspects of Glass Formation in Telluride Systems. *Journal of Non-Crystalline Solids* **1972**, *8*, 85-105.

6.   Kalikka, J.; Zhou, X.; Dilcher, E.; Wall, S.; Li, J.; Simpson, R. E., Strain-Engineered Diffusive Atomic Switching in Two-Dimensional Crystals. *Nature communications* **2016**, *7*, 11983.

7.   Zhao, J.; Hui, J.; Ye, Z.; Lai, T.; Efremov, M. Y.; Wang, H.; Allen, L. H., Exploring "No Man's Land"—Arrhenius Crystallization of Thin-Film Phase Change Material at 1 000 000 K S^{-1} Via Nanocalorimetry. *Advanced Materials Interfaces* **2022**, *9*, 2200429.

8.   Pashinkin, A.; Malkova, A.; Mikhailova, M., The Heat Capacity of Solid Antimony Telluride Sb2te3. *Russian Journal of Physical Chemistry A, Focus on Chemistry* **2008**, *82*, 878-879.

9.   Chase, M. W.; Organization, N. I. S., *Nist-Janaf Thermochemical Tables*; American Chemical Society Washington, DC, 1998; Vol. 9.

10.   Rocca, J.; Erazú, M.; Fontana, M.; Arcondo, B., Crystallization Process on Amorphous Getesb Samples near to Eutectic Point Ge15te85. *Journal of Non-Crystalline Solids* **2009**, *355*, 2068-2073.

11.   Pries, J.; Stenz, C.; Schäfer, L.; Gutsche, A.; Wei, S.; Lucas, P.; Wuttig, M., Resistance Drift Convergence and Inversion in Amorphous Phase Change Materials. *Advanced Functional Materials* **2022**, *32*, 2207194.

12.   Wei, S.; Coleman, G. J.; Lucas, P.; Angell, C. A., Glass Transitions, Semiconductor-Metal Transitions, and Fragilities in Ge− V− Te (V= as, Sb) Liquid Alloys: The Difference One Element Can Make. *Physical Review Applied* **2017**, *7*, 034035.

13.   Tsuchiya, Y., Thermodynamics of the Structural Changes in the Liquid Ge–Te System around the Te-Rich Eutectic Composition. *Journal of non-crystalline solids* **2002**, *312*, 212-216.

14.   Pries, J.; Weber, H.; Benke-Jacob, J.; Kaban, I.; Wei, S.; Wuttig, M.; Lucas, P., Fragile-to-Strong Transition in Phase-Change Material Ge$_3$Sb$_6$Te$_5$. *Advanced Functional Materials* **2022**, *32*, 2202714.

15.   Zhao, J.; Khan, A. I.; Ye, Z.; Efremov, M. Y.; Wu, X.; Wong, H.-S. P.; Pop, E.; Allen, L. H., Crystallization of Ge4sb6te7 Via Nanocalorimetry. *Manuscript in Preparation* **2023**.

16.   Pries, J.; Yu, Y.; Kerres, P.; Häser, M.; Steinberg, S.; Gladisch, F.; Wei, S.; Lucas, P.; Wuttig, M., Approaching the Glass Transition Temperature of Gete by Crystallizing Ge$_{15}$Te$_{85}$. *physica status solidi (RRL)–Rapid Research Letters* **2021**, *15*, 2000478.

17.   Pries, J.; Wei, S.; Wuttig, M.; Lucas, P., Switching between Crystallization from the Glassy and the Undercooled Liquid Phase in Phase Change Material Ge$_2$Sb$_2$Te$_5$. *Advanced materials* **2019**, *31*, 1900784.

18.   Lebaudy, P.; Saiter, J.; Grenet, J.; Belhadji, M.; Vautier, C., Identification of Amorphous Zones in the Getesb System. *Materials Science and Engineering: A* **1991**, *132*, 273-276.

19.   Legendre, B.; Hancheng, C.; Bordas, S.; Clavaguera-Mora, M., Phase Diagram of the Ternary System Ge-Sb-Te. I. The Subternary GeTe-Sb$_2$Te$_3$-Te. *Thermochimica Acta* **1984**, *78*, 141-157.

20.   Zhang, M.; Olson, E.; Twesten, R.; Wen, J.; Allen, L.; Robertson, I.; Petrov, I., In Situ Transmission Electron Microscopy Studies Enabled by Microelectromechanical System Technology. *Journal of materials research* **2005**, *20*, 1802-1807.

21.   Sun, S.; Peng, J.; Jin, R.; Song, S.; Zhu, P.; Xing, Y., Template-Free Solvothermal Synthesis and Enhanced Thermoelectric Performance of Sb2te3 Nanosheets. *Journal of alloys and compounds* **2013**, *558*, 6-10.

22.   Schulz, S.; Heimann, S.; Friedrich, J.; Engenhorst, M.; Schierning, G.; Assenmacher, W., Synthesis of Hexagonal Sb_2Te_3 Nanoplates by Thermal Decomposition of the Single-Source Precursor (Et2sb) 2te. *Chemistry of Materials* **2012**, *24*, 2228-2234.

23.   Dong, G.-H.; Zhu, Y.-J.; Cheng, G.-F.; Ruan, Y.-J., Sb_2Te_3 Nanobelts and Nanosheets: Hydrothermal Synthesis, Morphology Evolution and Thermoelectric Properties. *Journal of alloys and compounds* **2013**, *550*, 164-168.

24.   Howlett, B.; Bever, M.; Misra, S., On Thermodynamic Properties of Compounds Sb_2Se_3 Sb_2Te_3+ Bi_2Te_3. *Transactions of the Metallurgical Society of AIME* **1964**, *230*, 1367-&.

25.   Legendre, B.; Feutelais, Y.; Didry, J., Capacite Calorifique Molaire Du Compose $Sb_{0.405}$ $Te_{0.595}$ Dans Les Etats Solides Et Liquides Entre 298 K Et 922 K. *Journal of Thermal Analysis and Calorimetry* **1988**, *34*, 345-357.

26.   Da Silva, J. L.; Walsh, A.; Lee, H., Insights into the Structure of the Stable and Metastable (GeTe) M (Sb_2 Te_3) N Compounds. *Physical Review B* **2008**, *78*, 224111.

27.   Lai, S.; Guo, J.; Petrova, V.; Ramanath, G.; Allen, L., Size-Dependent Melting Properties of Small Tin Particles: Nanocalorimetric Measurements. *Physical review letters* **1996**, *77*, 99.